The following resources related to this article are available online at
www.sciencemag.org (this infomation is current as of October 17, 2011):

Updated information and services, including high-resolution figures, can be found in the online version of this article at:
http://www.sciencemag.org/content/333/6050/1723.full.html

Supporting Online Material can be found at:
http://www.sciencemag.org/content/suppl/2011/08/15/science.1209206.DC1.html

A list of selected additional articles on the Science Web sites **related to this article** can be found at:
http://www.sciencemag.org/content/333/6050/1723.full.html#related

This article **cites 26 articles**, 4 of which can be accessed free:
http://www.sciencemag.org/content/333/6050/1723.full.html#ref-list-1

elements of the nonlinear susceptibility tensors are not readily available. A consistent microscopic theory of the nonlinear response of polymers taking into account the molecular alignments and their electric activities is beyond the scope of this work. We conservatively estimate the efficiency of the plasmonic EFISH process to be 5.7×10^{-11} at $V_c = 20$ V. This value is on the same order magnitude as the conventional SHG conversion efficiency in a prototypical nonlinear crystal of the same thickness and under the same experimental conditions.

The plasmonic-EFISH devices demonstrated in this work can be generalized to other electrically controlled plasmonic frequency converters that are compact and relatively efficient and require no phase matching, rendering them suitable for chip-scale applications where integration is necessary.

References and Notes

1. R. Zia, J. A. Schuller, A. Chandran, M. L. Brongersma, *Mater. Today* **9**, 20 (2006).
2. H. A. Atwater, *Sci. Am.* **296**, 56 (2007).
3. M. L. Brongersma, V. M. Shalaev, *Science* **328**, 440 (2010).
4. R. Zia, M. D. Selker, P. B. Catrysse, M. L. Brongersma, *J. Opt. Soc. Am. A* **21**, 2442 (2004).
5. T. W. Ebbesen, C. Genet, S. I. Bozhevolnyi, *Phys. Today* **61**, 44 (2008).
6. W. S. Cai, W. Shin, S. H. Fan, M. L. Brongersma, *Adv. Mater.* **22**, 5120 (2010).
7. P. Mühlschlegel, H. J. Eisler, O. J. F. Martin, B. Hecht, D. W. Pohl, *Science* **308**, 1607 (2005).
8. E. S. Barnard, J. S. White, A. Chandran, M. L. Brongersma, *Opt. Express* **16**, 16529 (2008).
9. H. F. Schouten et al., *Phys. Rev. Lett.* **94**, 053901 (2005).
10. R. Zia, M. L. Brongersma, *Nat. Nanotechnol.* **2**, 426 (2007).
11. J. A. Schuller et al., *Nat. Mater.* **9**, 193 (2010).
12. A. Nahata, R. A. Linke, T. Ishi, K. Ohashi, *Opt. Lett.* **28**, 423 (2003).
13. P. Schön et al., *Opt. Lett.* **35**, 4063 (2010).
14. M. Airola, Y. Liu, S. Blair, *J. Opt. A* **7**, S118 (2005).
15. J. A. H. van Nieuwstadt et al., *Phys. Rev. Lett.* **97**, 146102 (2006).
16. M. W. Klein, C. Enkrich, M. Wegener, S. Linden, *Science* **313**, 502 (2006).
17. J. C. Quail, J. G. Rako, H. J. Simon, R. T. Deck, *Phys. Rev. Lett.* **50**, 1987 (1983).
18. W. Fan et al., *Nano Lett.* **6**, 1027 (2006).
19. K. Chen, C. Durak, J. R. Heflin, H. D. Robinson, *Nano Lett.* **7**, 254 (2007).
20. S. Kim et al., *Nature* **453**, 757 (2008).
21. M. Danckwerts, L. Novotny, *Phys. Rev. Lett.* **98**, 026104 (2007).
22. T. J. Xu, X. J. Jiao, S. Blair, *Opt. Express* **17**, 23582 (2009).
23. H. Harutyunyan, S. Palomba, J. Renger, R. Quidant, L. Novotny, *Nano Lett.* **10**, 5076 (2010).
24. P. Genevet et al., *Nano Lett.* **10**, 4880 (2010).
25. J. Leuthold, C. Koos, W. Freude, *Nat. Photonics* **4**, 535 (2010).
26. M. A. Foster et al., *Nature* **441**, 960 (2006).
27. R. W. Terhune, P. D. Maker, C. M. Savage, *Phys. Rev. Lett.* **8**, 404 (1962).
28. Materials and methods are available as supporting material on *Science* Online.

Coherent Two-Dimensional Nanoscopy

Martin Aeschlimann,[1] Tobias Brixner,[2,3]* Alexander Fischer,[1] Christian Kramer,[2] Pascal Melchior,[1] Walter Pfeiffer,[4] Christian Schneider,[1] Christian Strüber,[4] Philip Tuchscherer,[2] Dmitri V. Voronine[4]†

We introduce a spectroscopic method that determines nonlinear quantum mechanical response functions beyond the optical diffraction limit and allows direct imaging of nanoscale coherence. In established coherent two-dimensional (2D) spectroscopy, four-wave–mixing responses are measured using three ingoing waves and one outgoing wave; thus, the method is diffraction-limited in spatial resolution. In coherent 2D nanoscopy, we use four ingoing waves and detect the final state via photoemission electron microscopy, which has 50-nanometer spatial resolution. We recorded local nanospectra from a corrugated silver surface and observed subwavelength 2D line shape variations. Plasmonic phase coherence of localized excitations persisted for about 100 femtoseconds and exhibited coherent beats. The observations are best explained by a model in which coupled oscillators lead to Fano-like resonances in the hybridized dark- and bright-mode response.

In all implementations of optical spectroscopy, the spatial interaction volume has a lower bound determined by the diffraction limit of light. The laser focus diameter is always larger than roughly half the optical excitation wavelength, and measurements represent averages over a distribution of quantum systems present within the interaction volume. Single-emitter experiments are possible when only one quantum system contributes to the measurement signal through a combination of tight focusing and low emitter density. This method avoids ensemble averaging, and although ultrafast femtosecond experiments have recently been realized (1, 2), the spatial resolution is still diffraction-limited. Subdiffraction imaging resolution can be obtained via reversible fluorophore saturation such that only one emitter is active within the focal spot (3). This method works well for imaging but makes ultrafast spectroscopy challenging because the transitions need to be saturated. Near-field methods provide another way to achieve subdiffraction resolution (4), and ultrafast experiments have been performed (5). For these methods, one needs to implement raster scanning of the sample to obtain spatial-spectral information sequentially for each spot, and near-field two-dimensional (2D) spectroscopy has not yet been reported.

Here, we introduce coherent two-dimensional nanoscopy, which we define as the measurement of optical response functions using 2D spectroscopy with a spatial resolution below the optical diffraction limit. In contrast to potential near-field implementations, our technique uses wide-field illumination and detects 2D spectral information simultaneously for ~10^6 different spatial locations. In conventional 2D spectroscopy (6–9), the "input"

to a four-wave mixing scheme consists of three incident waves that create a transient coherence (i.e., third-order polarization), which is then radiated off as the "output." However, coherent detection is not necessarily required; fluorescence (10, 11) or electrons (12) can also be used. In coherent 2D nanoscopy, all four waves are input fields, and the output corresponds to excited electrons. The key
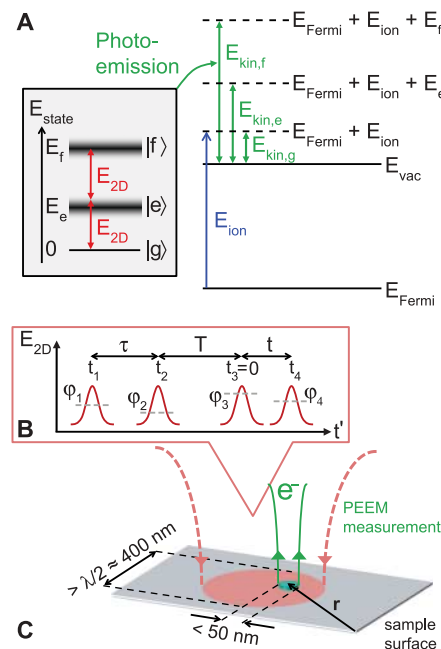

Fig. 1. Principle of coherent 2D nanoscopy. (**A**) Excitation of a quantum three-level system (left) leads to emission of photoelectrons with different kinetic energies (right). (**B**) A sequence of four femtosecond laser pulses is used for excitation. (**C**) The optical spot on the sample is larger than half the optical excitation wavelength (i.e., the diffraction limit), but photoemission electron microscopy (PEEM) provides 50-nm spatial resolution.

[1]Fachbereich Physik and Research Center OPTIMAS, Technische Universität Kaiserslautern, Erwin-Schrödinger-Str. 46, 67663 Kaiserslautern, Germany. [2]Institut für Physikalische und Theoretische Chemie, Universität Würzburg, Am Hubland, 97074 Würzburg, Germany. [3]Röntgen Research Center for Complex Material Systems, Am Hubland, 97074 Würzburg, Germany. [4]Fakultät für Physik, Universität Bielefeld, Universitätsstr. 25, 33615 Bielefeld, Germany.

*To whom correspondence should be addressed. E-mail: brixner@phys-chemie.uni-wuerzburg.de
†Present address: Institute for Quantum Science and Engineering, Texas A&M University, College Station, TX 77840, USA.

concept is that nonoptical detection does not suffer from the diffraction limitations of optical waves. We detect locally generated photoelectrons, and the spatial resolution is limited by the electron wavelength, which is three orders of magnitude smaller than the wavelength of a photon at an energy of 1 eV. Thus, 2D spectroscopy can be performed on a nanometer length and femtosecond time scale.

The principle of coherent 2D nanoscopy is illustrated in Fig. 1. Consider a quantum three-level system (Fig. 1A) consisting of a ground state $|g\rangle$, a first electronically excited state $|e\rangle$, and a second excited state $|f\rangle$. Transitions between the different levels are induced with an electric field E_{2D} consisting of four femtosecond subpulses (Fig. 1B) whose temporal separations can be varied and are labeled τ, T, and t, in analogy with 2D spectroscopy. In addition, the phases of the four subpulses, φ_i ($i = 1, \ldots, 4$), can be specified. This four-wave interaction leaves the system in one of the population states $|g\rangle\langle g|$, $|e\rangle\langle e|$, or $|f\rangle\langle f|$ that is probed via photoelectron emission. In general, $E_{state} = \{E_e, E_f\}$ might not exceed the work function, and additional energy can be supplied by an ionization laser of energy E_{ion}. For photoelectrons emitted from an initial state at the Fermi level, E_{Fermi}, the kinetic energy above vacuum level E_{vac} is given by $E_{kin} = E_{Fermi} + E_{ion} + E_{state} - E_{vac}$ (Fig. 1A). The horizontal dashed lines at the right of Fig. 1A therefore correspond to the maximum kinetic energy of the photoelectrons for given values of E_{ion} and E_{state}. The photoelectron yield is measured at a particular kinetic energy as a function of time delays τ, T, and t, and of relative phases φ_τ, φ_T, and φ_t. Coherent 2D spectra are then available via numerical Fourier transformation of the photoelectron yield with respect to τ and t (with population time T as a parameter). The general excitations can correspond either to states of collective nature, such as plasmon polaritons in metallic systems or excitons in molecular aggregates, or to single-particle states, such as distinct transitions in the electronic band structure. However, the probe process occurs via a single-particle state (i.e., the photoemission state). Because collective states cannot be represented on a single-particle energy scale, the quantum state preparation via the interaction with E_{2D} and the probe process are separated in Fig. 1A.

We used a time-resolved photoemission electron microscope (PEEM) to detect photoelectrons with a spatial resolution of 50 nm (13, 14) (fig. S3). The local nonlinear response function, rather than an averaged quantity, was measured as a function of position **r**. We did not detect outgoing optical fields, so the loss of four-wave–mixing phase matching was irrelevant. The simplest illumination geometry was fully collinear and allowed us to create the required pulse sequences with a femtosecond pulse shaper (15) that ensured phase coherence between the individual subpulses. We used phase cycling (10, 16)—that is, varying the phases φ_τ, φ_T, and φ_t and calculating suitable linear combinations of the signals—to retrieve the desired signal.

The Liouville-space pathways of 2D spectroscopy and 2D nanoscopy are completely analogous, although different linear combinations of them contribute to the final signal (14) (fig. S1). Electronic coherences are also measured in 2D nanoscopy despite the incoherent detection of electrons, and they can be analyzed with a response-function treatment (12, 17). The additional feature in 2D nanoscopy is the ability to access the general spatial-temporal response function (6).

We used this approach to study phase memory in metals. Single-particle electronic excitations in metals lose coherence within a few femtoseconds because of the continuous energy distribution of electronic states. However, plasmonic collective excitations at metal-dielectric interfaces exhibit longer phase memory (18). For localized surface plasmons investigated in nanostructured Ag samples (19, 20), dephasing times of $T_2 < 10$ fs have been reported. Rough metal surfaces display hot spots in photoemission for which the emission yield is strongly enhanced (21, 22) because of local field enhancement. This effect is also exploited in surface-enhanced Raman scattering (4). We used coherent 2D nanoscopy to study a silver surface, corrugated at the nanometer length scale and cleaned of surface contaminations by Ar$^+$ sputtering, to study such hot spots with 50-nm spatial resolution. For reasons of better signal statistics at limited available laser power, we used a simplified scheme without a separate ionization beam (14).

The real components of 2D nanospectra for two positions within the same hot spot are shown in Fig. 2, A and B. We observed line shapes that correspond to a single or very few contributing Lorentzian oscillators. The ultrahigh spatial resolution [at (18 nm)^2 detection area, which was binned for data evaluation to (36 nm)^2] eliminated to a large extent the inhomogeneous distribution of resonances that would be detected in diffraction-limited spectroscopy and that would lead to elongation of the 2D peak along the diagonal. Because the response varied spatially, the 2D line shapes were different even for two positions that were close together; for example, the diagonal width for $T = 0$ fs in Fig. 2A was greater than for a position only 228 nm away (Fig. 2B). Cuts of Fig. 2, A and B, along the diagonal (Fig. 2C, symbols) also showed the spatial differences.

We used a damped-oscillator model to simulate and fit the full 2D spectra [see (14) and fig. S2 for an exemplary comparison between experiment and simulation; the solid lines in Fig. 2C show diagonal cuts through the simulation data]. From the simulation we obtained a damping parameter of $\gamma = 0.023 \pm 0.003$ rad/fs for the first position and $\gamma = 0.012 \pm 0.001$ rad/fs for the second position, corresponding to coherence lifetimes of 43 fs and 84 fs, respectively; these are substantial differences given the expectations from literature (19, 20). Apart from these two exemplary locations, 2D spectra were calculated and fitted for each simultaneously recorded spatial location separately. A spatial line cut through

the hot spot revealed a position-dependent variation of the recovered lifetimes (Fig. 2D). Unexpected long lifetimes were detected, up to 10 times the values reported for localized plasmon modes in nanostructures (19, 20) (Fig. 2D). Additionally, we measured the coherence lifetime for the center of a different, "short-lived," hot spot that was located on the same sample but several micrometers away from the hot spot discussed here.

The spatial map (Fig. 2E) shows the deduced lifetimes for the complete hot-spot region together with the photoemission yield for a single pulse (contour lines). Note that areas with particularly long local coherence lifetimes did not exactly coincide with the highest photoemission yield (i.e., the contour-plot maximum). We could resolve a separation of ~100 nm between the point of highest emission and the longest lifetimes in its
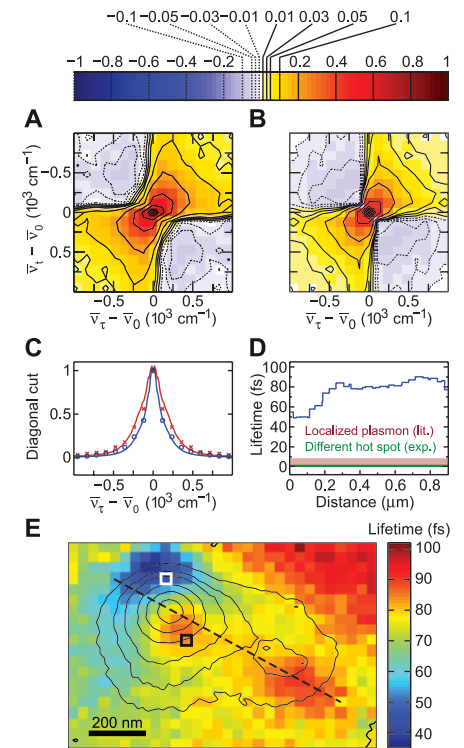

Fig. 2. Coherent 2D nanospectra. (**A** and **B**) The 2D real part is shown at $T = 0$ fs for one position (A) and another position (B) 228 nm away within the same hot spot, as a function of detuning from the center wave number $\bar{\nu}_0$ of the laser spectrum. $\bar{\nu}_\tau$ and $\bar{\nu}_t$ correspond to the frequencies related to the pulse delays τ and t, respectively. (**C**) Diagonal cuts emphasize the difference between (A) (red crosses) and (B) (blue circles), along with simulation data (lines). (**D**) The coherence lifetime is shown as a function of position (blue line) along with the measured lifetime of the center of a different hot spot (green) and the expected lifetime (19, 20) for a localized plasmon mode (red shaded). (**E**) The map indicates the coherence lifetimes (false colors) for the complete hot spot (photoemission yield in black contour lines). The white and black squares mark the locations of (A) and (B), respectively, and the dashed line indicates the cut shown in (D).

vicinity, which further demonstrated the spatial resolution of 2D nanoscopy. All spatial positions in Fig. 2E were recorded simultaneously under identical experimental conditions, so that line shape comparisons reflect true differences in sample response.

The observed long-lived coherences arise from the coupling of strongly damped localized plasmonic modes to dark plasmonic modes (Fig. 3A). Corrugations on the metal surface act as antennas for the incident light described by the electric field $\mathbf{E}(\mathbf{r},\omega)$ as a function of spatial coordinate $\mathbf{r}$ and angular frequency ω. Resonant excitation of localized plasmons leads to strong local field–enhanced multiphoton photoemission. Two electromagnetic field modes, $\mathbf{E}_1^{BM}$ and $\mathbf{E}_2^{BM}$, are required to model the observations; these couple strongly to the incident light (i.e., they act as bright modes) and exhibit a large spatial overlap with the bulk metal. Both effects lead to a strong damping and result in typical lifetimes on the order of ~10 fs (19, 20). These modes alone cannot account for the long coherence lifetime and its spatial variation (see Fig. 2). In contrast to short-lived localized plasmon modes, the surface plasmon polariton mode on a planar silver surface exhibits a coherence lifetime of ~200 fs for an 800-nm excitation wavelength, as estimated from the dielectric function of silver (23) and the surface plasmon polariton resonance condition (24). Surface plasmon polaritons neither couple directly to the far field nor have large overlap with bulk electronic states, hence their rather long coherence lifetime. How-

ever, because of the vanishing interaction with transverse radiation fields (i.e., incident light), the surface plasmon polariton mode is denoted as a dark mode and thus, on its own, cannot explain the observations of Fig. 2.

The model explaining the observed long-lived coherences is now based on the coupling between bright modes (i.e., the localized plasmon modes $\mathbf{E}_1^{BM}$ and $\mathbf{E}_2^{BM}$) and one spatially extended surface plasmon polariton $\mathbf{E}^{DM}$ that acts as a dark mode. The coupling strength between these modes is determined by the mode overlap inside the metal. Application of the hybridization model for plasmonic excitations (25), together with a mathematical model recently developed to describe plasmon-induced transparency in metamaterials (26) and adapted to the present situation, yield response functions for the hybridized plasmonic modes that can be used to model the experimentally observed spectroscopic signatures (14). Hybridization causes the response function of a bright mode to adopt characteristics of the dark mode—it strongly interacts with the incident radiation, and electronic excitations in the metal will exhibit spectral features that correspond to a much longer coherence lifetime, as would be expected for an uncoupled bright mode.

To support this qualitative model with experimental evidence, we conducted a two-pulse 2D nanoscopy scheme in which one pulse delay T was varied and for each delay the corresponding interpulse relative phase φ_T was scanned over the complete interval $[-\pi, \pi]$. Qualitatively, phase memory was apparent for those delays T for

which the signal varied with φ_T—that is, the signal depends on the "probe" phase with respect to the phase imprinted on the (quantum) system during excitation with the first pulse. Figure 3 shows the results for two closely spaced regions of interest (ROI 1 and ROI 2 in Fig. 3A, inset) within the same hot spot investigated in Fig. 2. Plots of experimental delay versus phase (Fig. 3, B and C, top) showed peak structures centered at $T = 0$ fs, $\varphi_T = 0$ rad, which extended to delays T greater than 200 fs. Without phase memory, the phase-dependent modulation of the photoemission signal would have vanished for a pulse separation greater than the pulse duration (50 fs). For example, in Fig. 3D, the emission from the other hot spot (whose very short coherence lifetime was already shown for comparison in Fig. 2D by the green line) rapidly decreased and reached a noise level of 10^{-3} for a delay of 100 fs. For the given nonlinear photoemission process, this response reflected a pure pulse autocorrelation and indicated that there was negligible local phase memory for that particular hot spot.

The signals for the investigated ROIs exhibited strikingly different phase dependences. The $\varphi_T = 0$ rad signal for ROI 1 (Fig. 3, B and D) decreased continuously, and outside of the pulse-overlap region, a lifetime of $\tau = 87$ fs could be fitted to an exponential decay. This number was in quantitative agreement with the lifetime values obtained from the 2D line shape analysis of Fig. 2. However, a nonmonotonic behavior was obvious for ROI 2 (Fig. 3, C and D), and more than one parameter was needed for a description. Similar coherent beats were also visible in Fig. 3B for $\varphi_T = -2$ rad.

The differences between ROI 1 and ROI 2 demonstrate that we can resolve spectral features that are separated spatially by less than the wavelength (i.e., from within an individual hot spot). The coherent beats indicate a local collective response that cannot be modeled by a single Lorentzian. Fit results using the coupled oscillator model (Fig. 3, B and C, bottom) showed good agreement with the experiment. These results indicated that the observed long-lived coherence in hot-spot multiphoton photoemission can indeed be attributed to the coupling between bright localized plasmon modes and a dark surface plasmon polariton mode. The corresponding hybridized response functions are displayed in Fig. 3E. Hence, the apparently single photoemission hot spot (Fig. 3A, inset) actually consisted of two bright modes $\mathbf{E}_1^{BM}$ and $\mathbf{E}_2^{BM}$ that were slightly detuned from the dark mode $\mathbf{E}^{DM}$ to higher and lower frequencies, respectively (Fig. 3E). Interestingly, the coupling between bright and dark modes led to Fano-like resonances in the vicinity of the resonance of the dark mode. The mirror-like behavior of this spectral feature for one versus the other bright mode was responsible for the striking differences in the signals shown in Fig. 3, B and C, and the variations in Fig. 2. Subtleties of the overlap of these spectral features with the excitation spectrum, such as the exact spectral position
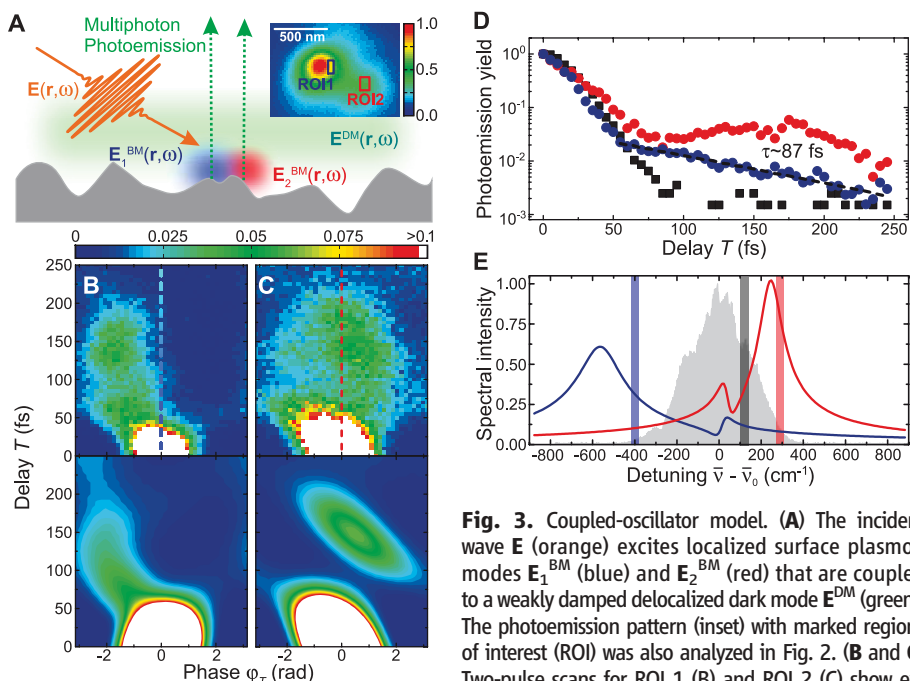

Fig. 3. Coupled-oscillator model. (**A**) The incident wave **E** (orange) excites localized surface plasmon modes $\mathbf{E}_1^{BM}$ (blue) and $\mathbf{E}_2^{BM}$ (red) that are coupled to a weakly damped delocalized dark mode $\mathbf{E}^{DM}$ (green). The photoemission pattern (inset) with marked regions of interest (ROI) was also analyzed in Fig. 2. (**B** and **C**) Two-pulse scans for ROI 1 (B) and ROI 2 (C) show experiment (top) and model fit (bottom). The data are normalized with respect to the emission at $T = 0$ fs and $\varphi_T = 0$ rad and then plotted on a color scale ranging from 0 to 0.1. The vertical dashed lines indicate cuts shown in (D). (**D**) Comparison of signals for $\varphi_T = 0$ rad from ROI 1 (blue circles) and ROI 2 (red circles) with another hot spot on the surface (black squares). (**E**) The derived response functions of the two hybridized modes $\mathbf{E}_1^{BM}$ (blue) and $\mathbf{E}_2^{BM}$ (red) are shown together with vertical shaded bars indicating the spectral positions of the uncoupled oscillators and the dark mode (gray bar). The excitation laser spectrum is indicated as shaded area.

and the "sharpness" of the Fano-like resonance, determined the observed beating behavior. This sensitivity of the model parameters for the two ROIs showed that the local response significantly varies on a 100-nm length scale, as was also seen for the coherence liftime measured by 2D nanoscopy.

The hybridization of localized modes with long-lived dark modes and the associated appearance of long-lived localized electronic coherence are of general interest for surface-enhanced spectroscopy. Moreover, the coupled-oscillator model connects the observation of long-lived coherences in hot spot–related multiphoton photoemission on corrugated surfaces to the intensively studied phenomenon of electromagnetically induced transparency in plasmonic systems (26–28). The observation and investigation of such coupled modes had been restricted to ensembles of identical structures (28, 29). With the application of 2D nanoscopy, we have resolved different Fano-like resonances within one individual hot-spot emission. Potential uses of 2D nanoscopy include polarization pulse shaping (30), which could allow mapping of the tensor character of the nonlinear response by selecting the appropriate polarization directions of the excitation sub-

pulses. Indeed, the pulse shapes themselves could be varied, allowing the combination of 2D nanoscopy and coherent control techniques. Higher-order processes and systems with more than three levels could be investigated with pulse trains consisting of more than four pulses. Extension to short wavelengths (12) should also be possible.

References and Notes
1. J. Kasprzak et al., Nat. Photonics **5**, 57 (2011).
2. D. Brinks et al., Nature **465**, 905 (2010).
3. S. W. Hell, Science **316**, 1153 (2007).
4. L. Novotny, B. Hecht, Principles of Nano-Optics (Cambridge Univ. Press, Cambridge, 2006).
5. T. Guenther et al., Phys. Rev. Lett. **89**, 057401 (2002).
6. S. Mukamel, Principles of Nonlinear Optical Spectroscopy (Oxford Univ. Press, New York, 1999).
7. S. Mukamel, Annu. Rev. Phys. Chem. **51**, 691 (2000).
8. D. M. Jonas, Annu. Rev. Phys. Chem. **54**, 425 (2003).
9. M. Cho, Chem. Rev. **108**, 1331 (2008).
10. P. Tian et al., Science **300**, 1553 (2003).
11. P. F. Tekavec, G. A. Lott, A. H. Marcus, J. Chem. Phys. **127**, 214307 (2007).
12. S. Rahav, S. Mukamel, Phys. Rev. A **81**, 063810 (2010).
13. O. Schmidt et al., Appl. Phys. B **74**, 223 (2002).
14. See supporting material on Science Online.
15. A. M. Weiner, Rev. Sci. Instrum. **71**, 1929 (2000).
16. S.-H. Shim, D. B. Strasfeld, Y. L. Ling, M. T. Zanni, Proc. Natl. Acad. Sci. U.S.A. **104**, 14197 (2007).
17. C. Timm, K. H. Bennemann, J. Phys. Condens. Matter **16**, 661 (2004).
18. W. A. Murray, W. L. Barnes, Adv. Mater. **19**, 3771 (2007).
19. N. Nilius, N. Ernst, H. Freund, Phys. Rev. Lett. **84**, 3994 (2000).
20. T. Hanke et al., Phys. Rev. Lett. **103**, 257404 (2009).
21. M. Aeschlimann et al., J. Chem. Phys. **102**, 8606 (1995).
22. R. C. Word et al., Appl. Phys. Lett. **96**, 251110 (2010).
23. P. B. Johnson, R. W. Christy, Phys. Rev. B **6**, 4370 (1972).
24. H. Raether, in Surface Plasmons on Smooth and Rough Surfaces and on Gratings, G. Höhler, E. A. Niekisch, Eds. (Springer, Berlin, 1988), pp. 1–133.
25. E. Prodan et al., Science **302**, 419 (2003).
26. S. Zhang et al., Phys. Rev. Lett. **101**, 047401 (2008).
27. N. Liu et al., Nat. Mater. **8**, 758 (2009).
28. B. Luk'yanchuk et al., Nat. Mater. **9**, 707 (2010).
29. C. Ropers et al., Phys. Rev. Lett. **94**, 113901 (2005).
30. T. Brixner, G. Gerber, Opt. Lett. **26**, 557 (2001).

Geometry and Mechanics in the Opening of Chiral Seed Pods

Shahaf Armon,[1] Efi Efrati,[1] Raz Kupferman,[2] Eran Sharon[1]*

We studied the mechanical process of seed pods opening in Bauhinia variegate and found a chirality-creating mechanism, which turns an initially flat pod valve into a helix. We studied configurations of strips cut from pod valve tissue and from composite elastic materials that mimic its structure. The experiments reveal various helical configurations with sharp morphological transitions between them. Using the mathematical framework of "incompatible elasticity," we modeled the pod as a thin strip with a flat intrinsic metric and a saddle-like intrinsic curvature. Our theoretical analysis quantitatively predicts all observed configurations, thus linking the pod's microscopic structure and macroscopic conformation. We suggest that this type of incompatible strip is likely to play a role in the self-assembly of chiral macromolecules and could be used for the engineering of synthetic self-shaping devices.

Motion in plants is a highly nontrivial process. It is often based on anisotropic swelling and shrinkage, driven by the relatively slow variation of water content within the tissue (1). Swelling and shrinkage may lead to the accumulation of elastic energy and the buildup of stress. This stress can be released via mechanical instabilities, such as fracture, buckling, and snapping (2, 3). The buildup of stress may also occur in sclerenchymal tissue (tissue made of dead cells) and is thus a process that can be analyzed from a purely

mechanical point of view. Sclerenchymal tissue typically consists of fiber cells whose walls are made of layered cellulose fibrils with a preferred orientation. When absorbing/expelling water, the tissue expands/shrinks anisotropically, perpendicularly to the fibrils' orientation [(1), p. 200]. Changes in air humidity induce such uniaxial swelling/shrinkage that drive, for example, the opening and closure of a pine cone (4) and the penetration of wheat seeds into soil (5).

Chiral pod opening is a nontrivial example of hygroscopic (humidity-driven) motion in sclerenchymal tissue. In this process, two initially flat pod valves curl into helical strips of opposite handedness. A detailed study of the structure of pod valves in over 300 species of Leguminosae shows a wealth of architectures (6). We studied pod opening in Bauhinia variegate (Fig. 1, A and B),

whose pod valves are known to consist of two fibrous layers, oriented roughly at ±45° with respect to the pod's longitudinal axis [supporting online material (SOM) text and fig. S1, x-ray scattering measurements and fig. S2]. It turns out that the mere presence of two layers that shrink in perpendicular directions is sufficient to drive the flat-to-helical transition in pod opening.

As a proof of concept, we constructed a mechanical analog of the Bauhinia pod that copies its geometry. We stretched two identical thin latex sheets uniaxially by the same elongation factor. We then glued one on top of the other in perpendicular directions (Fig. 1C). Once released from the external stretching, the composite object underwent the same shrinkage profile as the Bauhinia valve: The two layers shrunk uniaxially in perpendicular directions. Elongated strips cut out from the composite sheets were found to curl into helical configurations (Fig. 1F).

It is well known that uniaxial shrinkage of one layer in a bilayered sheet induces curvature, which accommodates the difference in length of the two layers. When the sheet is thin enough, it bends accordingly. Strips with a single intrinsic curvature have been studied extensively; large sheets adopt a cylindrical configuration, whereas narrow strips adopt helical configurations that are "cut from a cylinder" (7–10).

A qualitatively different situation occurs when two layers shrink perpendicularly. In such a case, the sheet "wants" to bend in two opposite and perpendicular directions—that is, they locally assume a saddle-like configuration (Fig. 1, D and E). This tendency to bend into a saddle creates a

[1]Racah Institute of Physics, Hebrew University of Jerusalem, Jerusalem 91904, Israel. [2]Institute of Mathematics, Hebrew University of Jerusalem, Jerusalem 91904, Israel.

*To whom correspondence should be addressed. E-mail: erans@vms.huji.ac.il